Optimal Design of a Variable-Twist Tiltrotor Blade Using Shape Memory Alloys

Jae-Sang Park
Research professor
Department of Aerospace Information Engineering,
Konkuk University

Seoul, KOREA
smartrotor@gmail.com

Seong-Hwan Kim
Graduate student
Department of Aerospace Information Engineering,
Konkuk University

Seoul, KOREA
ogmaksh@naver.com

Sung Nam Jung
Professor
Department of Aerospace Information Engineering,
Konkuk University

Seoul, KOREA
snjung@konkuk.ac.kr

Abstract

The tiltrotor blade, proprotor, acts as a rotor in helicopter mode and a propeller in airplane mode. For the best performance, each flight mode requires different built-in twist distributions of a proprotor, therefore the variable-twist proprotors have been proposed. This paper constructs an optimization framework for designing the cross-sections of a new variable-twist proprotor using shape memory alloy hybrid composites (SMAHC) containing shape memory alloy (SMA) wires embedded in the composite matrix. The present optimal design attempts to find the cross-section internal layout which maximizes the twist actuation of the new variable-twist proprotor while satisfying a lot of design constraints. The framework is constructed by integrating the various analysis and design tools such as an active composite cross-sectional analysis, a nonlinear flexible multibody dynamics analysis, a 3D strain analysis and a gradient-based optimizer. The design result shows that the twist actuation of the variable-twist proprotor can be maximized with that the design constraints are satisfied.

Introduction

The tiltrotor aircraft is a highly attractive and versatile vehicle since it has the capability of vertical take-off/landing and high-speed flight. The vehicle consists of three operation modes: helicopter mode, transition mode and airplane mode. Also called a proprotor, the tiltrotor blade can function as a helicopter rotor blade in the helicopter mode and as a propeller in the airplane mode. Because of the dual function, the proprotor experiences two different aerodynamic environments. In the helicopter mode, it has a relatively small inflow, high blade loading and a high rotor speed, whereas in the airplane mode, it has a high inflow, small blade loading and a relatively low rotor speed. The difference in the inflows and rotor speeds between the two flight modes necessitates that the proprotor requires a low built-in twist for the helicopter mode but a high built-in twist for the airplane mode for a good performance. Because of their conflicting requirements, the built-in twist is determined conventionally from a compromise between the two built-in twist angles adequate for the helicopter and airplane modes,

respectively. Naturally, this conventional design method is unable to guarantee the best performance of both the helicopter mode and the airplane mode.

Several researchers have studied the variable-twist proprotor concept to overcome this problem. The most successful approach to date involves taking advantage of the anisotropic nature of fiber-reinforced composite materials. By using elastically-tailored composite blades, a coupling between the extension and the torsion can be achieved. In this method, the different levels of centrifugal forces caused by the different rotor speeds in the helicopter and the airplane modes are used to change the built-in twist distribution [1-3]. This approach moderately or significantly reduces the rotor power for hover and slightly increases the axial efficiency for cruise. However, since this approach is based only on a passive control method, the adaptive control of the built-in twist is difficult to achieve under different flight conditions. Although smart materials are widely used for structural controls, only a limited number of studies have been examined the use of smart materials for a variable-twist proprotor. The twist performance of a shape memory alloy (SMA) actuator with a torque tube configuration is promising [4]. The first

research for the proprotor design and the performance improvement analysis through the variable-twist control using the SMA was conducted by the authors [5]. In the work, SMA hybrid composites (SMAHC) as an SMA actuator which consist of SMA wires and composite matrix were used as given in Figure 1. Through the SMAHC actuation by heating, the proprotor performance could be improved adaptively with respect to the different thrust level conditions in hover. However the variable-twist proprotor in that research was designed by a manually iterative process. Thus the twist actuation with a given temperature change to the SMAHC could not be maximized, although the maximization of a twist actuation is extremely important for an efficient variable-twist control.
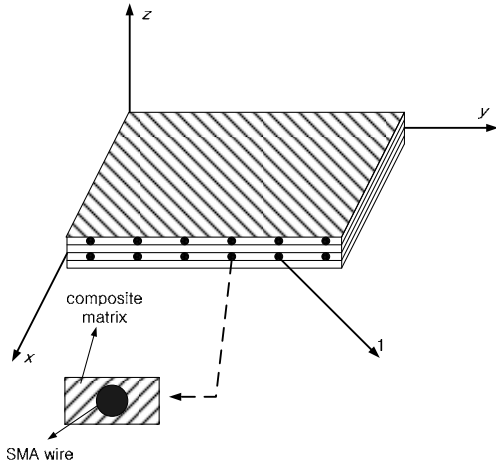
Figure 1 Shape memory alloy hybrid composites (SMAHC)

So far, there have been numerous studies for optimal designs for the composite proprotor and rotor blades [2, 3, 6-8] and active twist rotor blades utilizing anisotropic piezoelectric composite actuators [9, 10]. However no studies have been carried out for the optimal design of the variable-twist proprotor using SMA. Therefore the present work conducts the design optimization for the variable-twist proprotor with the SMAHC. The present proprotor is designed based on the proprotor of the KARI (Korea Aerospace Research Institute) SUAV (Smart Unmanned Aerial Vehicle, [11]) tiltrotor as shown in Figure 2. The behaviors of an SMA wire for the SMAHC are predicted by Brinson model [12] and the effective material properties of an SMAHC prepreg are obtained from the rule of mixture. The design optimization framework is composed of various analysis and design tools such as an active composite cross-sectional analysis, a nonlinear flexible

multibody dynamics analysis, a 3D strain analysis and a gradient-based optimizer. All of these codes are integrated closely by MATLAB. The static tip twist is selected as an objective function in this optimal design study. The design result exhibits that the tip twist can be maximized while satisfying a series of design constraints.

Figure 2 KARI SUAV tiltrotor [11]

Technical Approach

Thermomechanical behavior of an SMA wire

Brinson model [12] is used to simulate the thermomechanical behavior of an SMA wire. This model utilizes the rate constitutive equation which was already used in previous models by Tanaka [13] and Liang-Rogers [14]. However the martensite volume fraction ξ in Brinson model is divided into two components of the stress-induced ξ_S and the temperature-induced ξ_T martensite volume fractions, and $\xi = \xi_S + \xi_T$. The constitutive equation is expressed as

$$\sigma - \sigma_0 = E(\xi)(\varepsilon - \varepsilon_0) + \Omega(\xi)(\xi_S - \xi_{S_0}) + \Theta(\xi)(T - T_0) \quad (1)$$

where the subscript '0' indicates the initial condition. The detailed expressions of ξ_S and ξ_T in the phase transformations are given in Ref. [12]. In addition, E, Ω and Θ are Young's modulus, the thermoelastic coefficient, and the phase transformation coefficient, respectively and they are represented as

$$\begin{aligned} E(\xi) = E_A + \xi(E_M - E_A) \quad & \Omega(\xi) = -\varepsilon_L E(\xi) \\ \Theta(\xi) = \Theta_A + \xi(\Theta_M - \Theta_A) \quad & \Theta(\xi) = \alpha(\xi)E(\xi) \end{aligned} \quad (2)$$

where ξ_L and α are the maximum residual strain and the thermal expansion coefficient, respectively. Furthermore, the subscripts 'A' and 'M' denote the austenite phase and the martensite phase, respectively.

Effective material properties of SMAHC

For the SMAHC the SMA wires are embedded into composite matrix in the fiber. The effective material properties of an SMAHC are predicted by the rule of mixture [15] as

$$E_1 = E_{1m}V_m + E_sV_s \qquad E_2 = \frac{E_{2m}E_s}{\left(E_{2m}V_s + E_sV_m\right)}$$

$$G_{12} = \frac{G_{12m}G_s}{\left(G_{12m}V_s + G_sV_m\right)} \qquad v_{12} = v_{12m}V_m + v_sV_s \qquad (3)$$

$$\rho = \rho_mV_m + \rho_sV_s$$

where the subscripts 'm' and 's' mean the composite matrix and SMA wire, respectively. Young's modulus, shear modulus, and Poisson's ratio of an SMAHC lamina are represented as E, G, and v, respectively. The material density of an SMAHC prepreg is given as ρ. In addition, V_m and V_s are the volume fractions of the composite matrix and SMA wires, respectively.

The constitutive equation of the k-th SMAHC lamina is given as

$$\boldsymbol{\sigma}_k = \bar{\mathbf{Q}}_k\boldsymbol{\varepsilon} + \boldsymbol{\sigma}_{r_k}V_{s_k} \qquad (4)$$

where $\boldsymbol{\sigma}_r$ is the recovery stress vector of an SMA wire obtained from the Brinson model and $\bar{\mathbf{Q}}$ is the transformed reduced stiffness matrix of an SMAHC. It is assumed that the temperature change to actuate SMA wires is applied to SMA wires solely and the thermal expansion effect of an SMA wire is already included in the recovery stress $\boldsymbol{\sigma}_r$. The second term represents the recovery stress of an SMAHC prepreg.

Cross-section modeling of the variable-twist proprotor for optimal design

The present variable-twist proprotor is designed optimally based on the KARI SUAV proprotor. The general properties of the baseline proprotor [11] are given in Table 1 and more detailed information can be found Ref. [16]. The present variable-twist proprotor utilizes the geometric configuration of the baseline proprotor without modification. However a new proprotor uses SMAHC plies which are distributed from 40 to 93% blade span as given in Figure 3.

The general cross-section configuration of the variable-twist proprotor for the present optimal design is shown in Figure 4. The cross-sections at

40%, 60%, 85%, and 93%R are considered for the design. Though the present variable-twist proprotor maintains the external configuration of the baseline proprotor, the present internal cross-section layout is newly designed as follows.

Table 1 General properties of the KARI SUAV proprotor [11]

Number of rotors	2
Number of Blades per rotor, N	3
Rotor type	Stiff-inplane
Rotor radius, R	1.432 m (4.70 ft)
Mean chord length, c	0.177 m (0.58 ft)
Solidity, σ	0.118
Airfoil sections	SF30, SF25, SF18, SF12, SF08
Blade built-in twist	Nonlinear -38°
Hub type	Gimbal
Rotor RPM, Ω	1284 RPM (Airplane)
	1605 RPM (Helicopter)
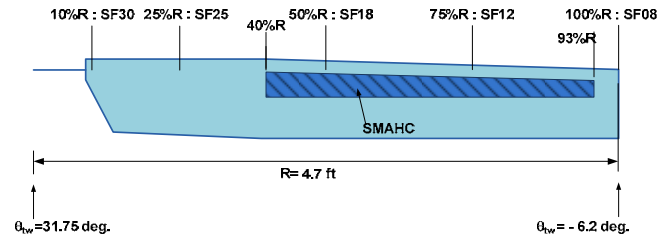
Figure 3 Planform of the variable-twist proprotor
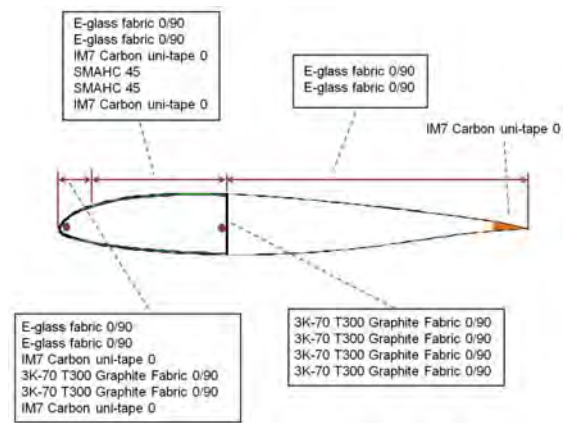
Figure 4 General layup configuration of the variable-twist proprotor

The skin consists of two E-glass fabric plies, and two SMAHC plies are inserted between two IM7 Carbon uni-

tape plies in the spar. Nitinol alloy wires and S-glass composite materials are used as SMA wires and composite matrix, respectively for the SMAHC prepreg. The volume fraction of Nitinol alloy wires is fixed as 0.3 in this design. Since the initial built-in twist of the variable-twist proprotor is for the airplane mode, the SMAHC should twist the proprotor in the pitch-up direction for the helicopter mode, which reduces the built-in twist. Due to this requirement, the SMAHC plies are embedded in 45 deg. with respect to the rotor blade axis. Furthermore, 3K-70 T300 Graphite fabric plies are used for the web structure and the nose region. To match the baseline blade weight and locate the center of gravity (C.G.) around the quarter chord position, two tungsten ballast weights are used, and their weights and locations are determined from the optimization. In addition, IM7 Carbon uni-tape is inserted into the trailing-edge to make the 1st lead-lag frequency (1L) of a proprotor blade to be higher than 1/rev (1P) for a stiff-inplane rotor.

Design optimization framework

The optimization problem to maximize the tip twist actuation of the variable-twist proprotor using the SMAHC can be expressed as

$$\max_{x} f(x) \qquad (5)$$

subject to

$$g(x) \le 0 \qquad (6)$$
$$x_l \le x \le x_u \qquad (7)$$

where f is an objective function which is the static tip twist due to the actuation of the SMAHC plies and x is a vector of the design variables. In addition, $g(x)$ is the set of nonlinear constraints, x_l and x_u are lower and upper bounds of x, respectively.

As design variables, the start/end locations of SMAHC plies, the locations of two ballast masses and their weights are selected as shown in Figure 5. For simplicity, the location of the web is assumed to be coincident with the end location of SMAHC plies.

Regarding the constraints in the proposed framework, the blade mass per unit length, the blade flapwise/chordwise bending stiffness, the chordwise locations of the center of gravity and the elastic axis, the 1st leadlag frequency of the proprotor in cyclic mode, and the maximum allowable blade local strain under the worst-case loading condition are

considered. In addition to these, few additional constraints are added for more realistic design.
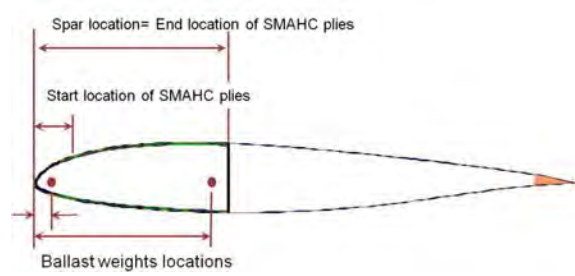
Figure 5 Design variables for optimization study

The proposed framework for an optimal design is schematically described in Figure 6. The framework consists of various numerical tools: UM/VABS (University of Michigan/Variational-Asymptotic Beam Cross-Sectional Analysis, [17]), an automated mesh generator [18], DYMORE [19], a MATLAB based 3-D strain analysis module, and a gradient based optimizer provided by MATLAB Optimization Tool Box [20]. These tools are integrated tightly by MATLAB.
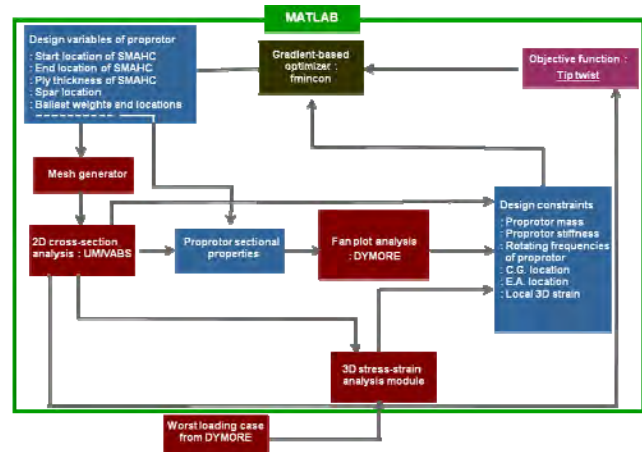
Figure 6 Flowchart of a proposed design optimization framework for variable-twist proprotor

UM/VABS based on a finite element method is used to determine the proprotor sectional properties such as the stiffness and inertial matrices, the chordwise locations of center of gravity and shear center, and the actuation forces/moments and deformations. Although UM/VABS input has a NASTRAN-based format, this work uses an automated mesh generator which is written in MATLAB since UM/VABS is included in the optimization framework. The mesh generator takes a few input parameters and creates meshes. To generate a general airfoil surface, contour equations for NACA four- and five-digit series airfoils or direct input of airfoil

coordinates are implemented. With a generated airfoil surface, layup configuration using given passive and active materials is defined. Through a table look-up, material properties are loaded for each layer. Although UM/VABS may analyze any type of internal cross-section components, the present mesh generator can only create meshes for the outer-shells and webs. The inertial effects of the ballast masses and the stiffness effect of the IM7 Carbon uni-tape at the trailing-edge are added directly to the inertia and stiffness matrices obtained from UM/VABS, respectively. Their effects are also considered when the locations of C.G. and shear center are determined. The obtained sectional properties are substituted into a nonlinear flexible multibody dynamic analysis.

Another important tool in the present framework is a nonlinear flexible multibody dynamics analysis code, DYMORE, to investigate the rotating frequencies of the proprotor blade. Also it is used to analyze the structural loads of the baseline proprotor blade for the worst-case loading outside the framework. The proprotor blade loads in a transition flight with nacelle angle 60 deg. which is known as the most severe loading condition for the baseline proprotor [21] are passed on to a 3D strain analysis for the structural integrity investigation. DYMORE is able to construct a multibody modeling using rigid/elastic joints, rigid bodies, and nonlinear elastic bodies such as beams, plates, and shells. Furthermore it has simple aerodynamic models based on the lifting line theory for rotors and wings. This powerful multibody modeling capability of DYMORE is very effective at representing complicated rotor systems elaborately, although DYMORE has not been specially developed for rotor comprehensive analysis. The brief modeling techniques for the proprotor system are described as follows.

Figure 7 shows the multibody modeling for an isolated proprotor system. The detailed view of hub and control system is given in Figure 8. The proprotor blades are modeled as nonlinear elastic beams considering the coupled flap, lead-lag and torsion behaviors. The geometrically nonlinear beam theory [22] is used for a nonlinear elastic beam modeling. The proprotor blade consists of flexures, spindles, and outer blades. Each flexure, spindle, and outer blade is discretized into 5, 5, and 10 finite elements with the third-order polynomials, respectively. Three blades are joined at the hub which is modeled as a rigid body with joints for the prescribed rotation and gimbal motion. Sophisticated rotor control system modeling is introduced. The pitch horns and the swashplates are modeled as rigid bodies, and a pitch link with a linear spring is

considered to give the control system some flexibility. The relationship between the swashplate movement and the collective pitch angle is nonlinear, unlike in general helicopters; hence, swashplate movement based on the test results for the baseline proprotor is prescribed. The pylon is modeled as an elastic beam with rigid sectional properties. To consider an isolated proprotor system, the clamped boundary condition is applied to the end of the pylon. For the loads analysis of the proprotor blade conducted outside the framework, the modeling for the aerodynamic loads on the blade and the trim analysis modeling are added to the proprotor structural modeling. For the aerodynamic loads on the proprotor, the finite-state dynamic inflow model [23] is used. This model is constructed by applying the acceleration potential theory to a rotor aerodynamics problem with a skewed cylindrical wake. More specifically, the induced flow at the rotor disk was expanded in terms of its modal functions. As a result, a three-dimensional, unsteady induced-flow aerodynamics model with a finite number of states is derived in the time domain. The total 21 airstations are located on each blade and C81 tables are employed. The trim analysis in DYMORE is conducted by autopilot theory, and the thrust and the two 1st harmonic components of the flapping angle in a given flight condition are considered as the trim target values in this modeling.
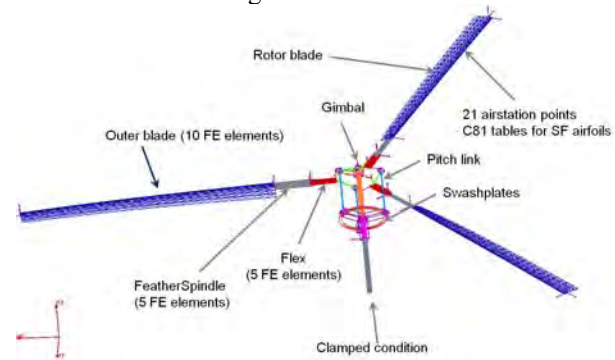
Figure 7 Multibody modeling for
an isolated proprotor system
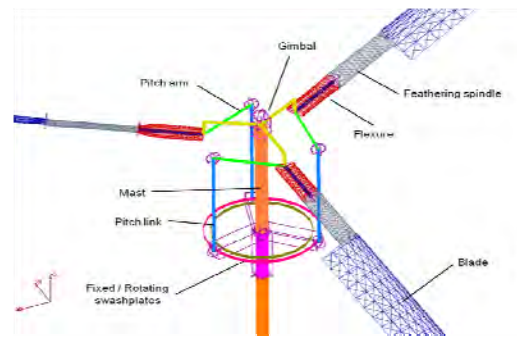
Figure 8 Detailed view of multibody modeling for
proprotor system

When the proprotor blade structural loads in the worst-case loadings and the sectional properties are obtained, a MATLAB-based 3D strain analysis is conducted to investigate the blade structural integrity. The structural loads and the centrifugal force from the fan plot analysis are used with the strain influence matrix from UM/VABS analysis to recover the local 3D strain components of the composite/active layers at every cross-section point of the cross-sections. The proprotor blade loads analysis with updated sectional properties should be conducted at each design iteration step, however the structural loads for the baseline proprotor blade which are calculated outside the framework are fixed during the optimization iterations for simplicity and efficiency. The safety factor of 1.5 is selected. The maximum strain criterion is applied for each component in the resulting strain and it is compared with the allowable values for the local constituent materials.

Finally as a mathematical optimization algorithm, the gradient-based constrained optimizer of the 'fmincon' command provided in MATLAB Optimization Toolbox is integrated with the aforementioned analysis tools. This optimizer attempts to find a constrained minimum of a scalar function composed of several variables starting with an initial estimate. This is generally referred to as constrained nonlinear optimization. For a medium-scale optimization problem, the 'fmincon' function uses a Sequential Quadratic Programming (SQP) method. Based on that method, the present command solves a Quadratic Programming (QP) sub-problem at each iteration step. An estimate for the Hessian of the Lagrangian is updated at each iteration step using the BFGS formula [24]. Three types of termination criteria are provided: the maximum number of iterations, the tolerance of the design variables, and the tolerance of the function value. When one of these termination criteria is satisfied, the optimization iteration will be finished.

Numerical Results

Thermomechanical behavior of an SMA wire

The thermomechanical behavior of the SMA wire is analyzed using the Brinson model, and the present results are compared with those by Brinson [12]. A typical Nitinol alloy wire [12] is used as the SMA wire, and Table 2 shows the thermomechanical properties of the wire.

Figure 9 depicts the stress-strain curve of the Nitinol alloy wire showing the pseudoelastic effect and the shape memory effect. It is seen that the present predictions are in excellent agreement with the results in Ref. [12]. The pseudoelastic effect can be observed in the curves for $T=40°C$ and $60°C$. Because the temperature ($T=40°C$) is lower than the austenite finish temperature (A_f), the curve for $T=40°C$ shows a partial pseudoelastic strain recovery at unloading. The curve for $T=60°C$ exhibits a complete strain recovery at unloading because the temperature ($T=60°C$) is higher than the austenite finish temperature (A_f). The other two curves for $T=12°C$ and $20°C$, which are below the austenite start temperature (A_s), illustrate the shape memory effect. When the load is eliminated, residual strains exist in both curves. These residual strains at zero stress can disappear when the temperature is raised above the austenite finish temperature (A_f), which is defined as the shape memory effect and an example is given in Figure 10. As seen in the figure, the present simulation correlates well with the previous results and the residual strain becomes zero when the temperature is increased above the austenite finish temperature (A_f). Figure 11 shows the recovery stress of the Nitinol alloy wire produced from this shape memory effect. As with the previous examples, the present prediction is in good agreement with the reference results. When the phase transformation starts, the recovery stress is increased linearly. After the phase transformation is completed, the recovery stress remains constant. In addition, there is a hysteresis loop during the heating and cooling processes. The recovery stress of the Nitinol alloy wire during heating is used to change the built-in twist of the proprotor.

Table 2 Material property of the Nitinol alloy wire [12]

Property	Value
E_M	26.3 GPa
E_A	67.0 GPa
Θ	0.55 MPa/°C
M_f	9 °C
M_s	18.4 °C
A_s	34.5 °C
A_f	49 °C
C_M	8 MPa/°C
C_A	13.8 MPa/°C
σ_s^{cr}	100 MPa
σ_f^{cr}	170 MPa
ε_L	0.067
ρ^*	6000 kg/m^3

*: typical value is used
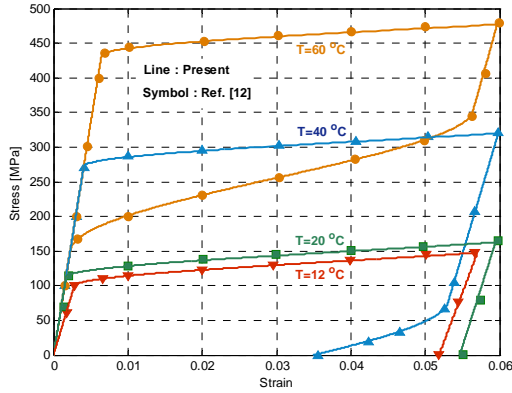
Figure 9 Thermomechanical behavior prediction for the Nitinol alloy wire
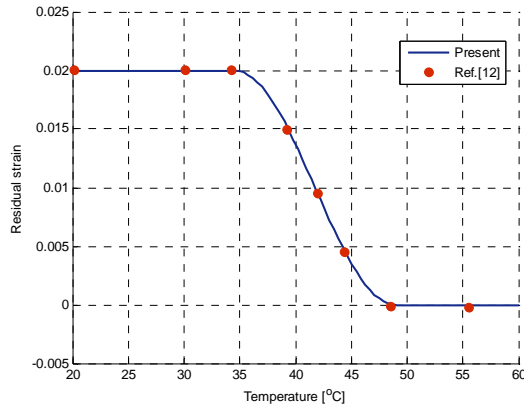
Figure 10 Relationship between residual strain and temperature for shape memory effect
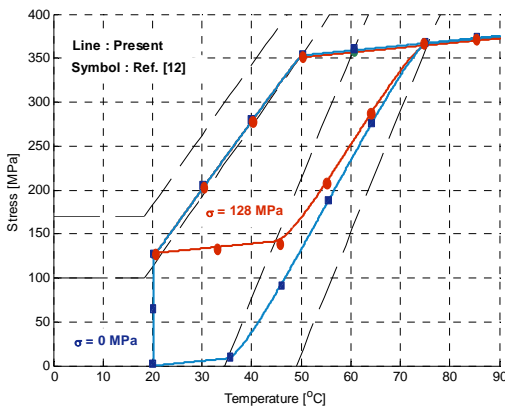
Figure 11 Recovery stress for shape memory effect

Design optimization results of the variable-twist proprotor using SMAHC

In this section, the design optimization using the proposed framework is conducted for the variable-twist proprotor with the SMAHC. This optimization example considers the start/end locations of the SMAHC of the 4 sections at 40%(section 1), 60%(section 2), 85%(section 3), and 93%R(section 4) , the weights of the two ballast masses and their locations as design variables. To reduce the number of design variables, it is assumed that the weights and the locations of the two ballast masses are constant along the blade span. Thus the total number of design variables is 12 in this study. Table 3 gives the initial values of the design variables which are selected based on the first author's experience on the previous study [5]. However the proprotor blade with these initial design variables does not indicate exactly the proprotor blade in the previous design [5]. In addition, as previously described, a series of design constraints and bounds are considered for the aeroelastic stability, the structural integrity, to match the baseline KARI SUAV proprotor characteristics and for the feasible solution, and they are summarized in Table 4.

Table 3 Initial values for the design variables

Start locations of SMAHC	$0.0455c$ (section 1)
	$0.0455c$ (section 2)
	$0.0455c$ (section 3)
	$0.0025c$ (section 4)
End locations of SMAHC	$0.4000c$ (section 1)
	$0.3550c$ (section 2)
	$0.2900c$ (section 3)
	$0.2570c$ (section 4)
Ballast masses (slug)	$(0.0049, 0.0049)$
Ballast mass locations	$(0.0c, 0.4c)$

Table 4 Design constraints and bounds

Center of gravity	$0.22c \leq$ C.G. $\leq 0.28c$
Elastic axis	$0.22c \leq$ E.A. $\leq 0.28c$
Blade mass/length	$0.95 \leq m/m_{baseline} \leq 1.05$
Flapwise bending stiffness	$0.95 \leq EI_{flap}/EI_{flap\ baseline} \leq 1.10$
Chordwise bending stiffness	$0.95 \leq EI_{chord}/EI_{chord\ baseline} \leq 1.10$
1st leadlag frequency in cyclic mode	$1L \geq 1.25$/rev at 1605 RPM
Local strain in the worst-case loading	Max. strain < ultimate strength of the constituent material
Start/ end locations of SMAHC region	$0.0455c \leq$ Location $\leq 0.85c$

Figure 12 shows the convergence history of an objective function: tip twist angle when the applied temperature

change to the SMAHC is 40°*C*. The reference value means the tip twist angle in the previous study [5]. As seen in the figure, a total of 26 iterations are required to get the converged solution, and there are 3 discontinuities at the 5, 14, and 18th iteration. After the convergence, the tip twist angle is approximately 3.9 deg. which is improved by 8% as compared with the reference twist value.
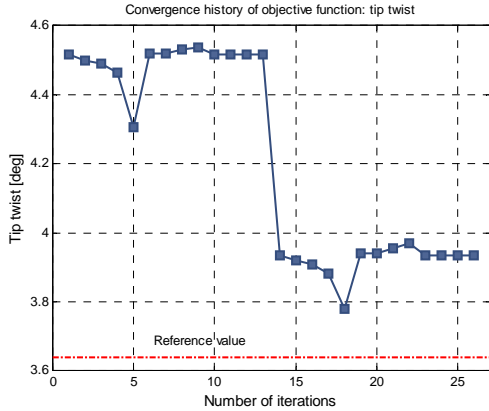
Figure 12 Convergence history of the objective function: tip twist

Figure 13 illustrates the convergence histories of the mass per unit length, the flapwise bending stiffness, the chordwise bending stiffness and the torsional stiffness of the 4 sections. All the values are normalized with respect to the corresponding baseline values. After the convergence is completed, all the sectional masses are designed to be maintained nearly as the baseline values. For the sectional flapwise bending stiffness, the flapwise bending stiffness of the section 1 is increased by about 9%, but the other sectional flapwise bending stiffness are retained as the reference values. All the chordwise bending stiffness have extremely similar values to the baseline values. This is because IM7 Carbon uni-tape at the trailing-edge is used appropriately to match the reference values. It is noticeable that the sectional torsion stiffness of all the sections are designed to be reduced significantly, which will facilitate the variable-twist control.

The convergence history of the 1st leadlag frequency in the cyclic mode at 1605 RPM is illustrated in Figure 14. As seen in the figure, the converged frequency satisfies the constraint that the 1st leadlag frequency should be higher than 1.25/rev to be the stiff-inplane rotor. Furthermore, it is observed that there are the two discontinuity regions where agree with the two discontinuity regions in Figure 13(a).

Figure 15 depicts the optimization history of the start/end locations of the SMAHC region. The start/end locations in the section 1 and the start location in the section 3 are moved to the backward moderately from the initial locations, but the other locations are located at the initial locations nearby. Although the start/end locations of the SMAHC region in some sections are changed from the initial locations, its whole coverage area is not much changed as compared with the initial coverage area.
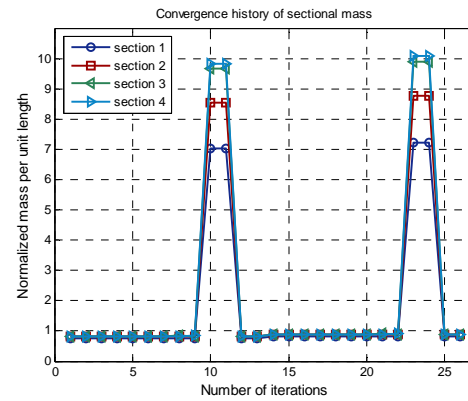
(a) Sectional mass per unit length
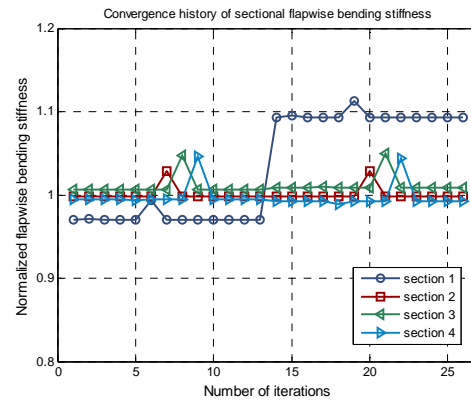
(b) Sectional flapwise bending stiffness
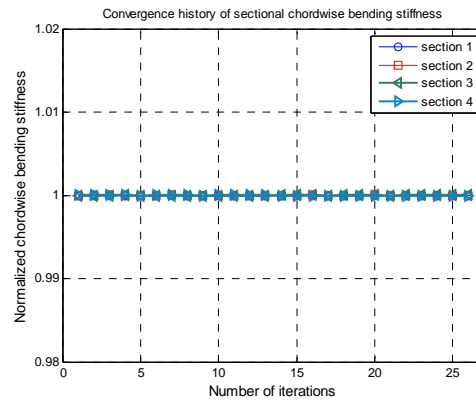
(c) Sectional chordwise bending stiffness
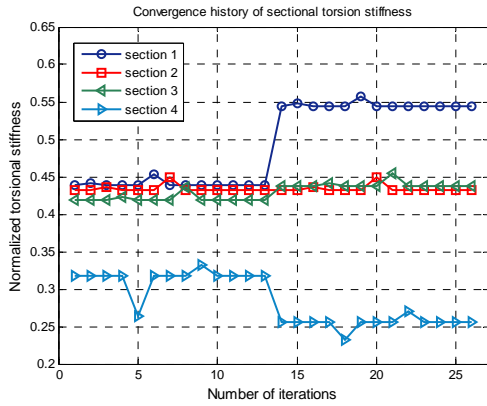
(d) Sectional torsion stiffness

Figure 13 Convergence histories of the normalized sectional properties
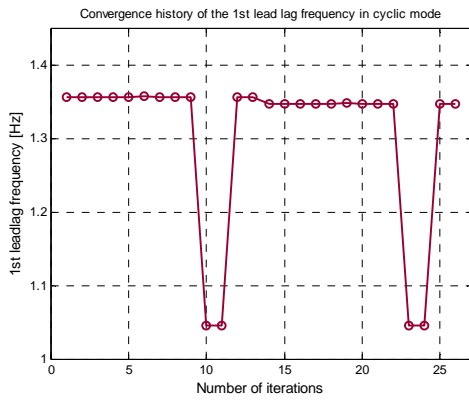
Figure 14 Convergence history of the 1st leadlag frequency in cyclic mode (1605 RPM)
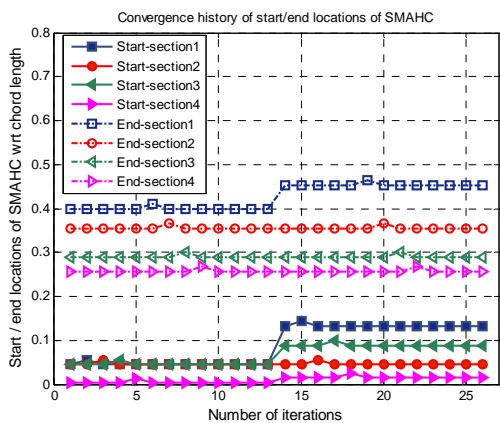
Figure 15 Convergence histories of the start/end locations of SMAHC regions

Figure 16 gives the optimization history of the locations of two ballast weights. As seen in the figure, the two locations remain closely to the initial locations during the whole iteration process.
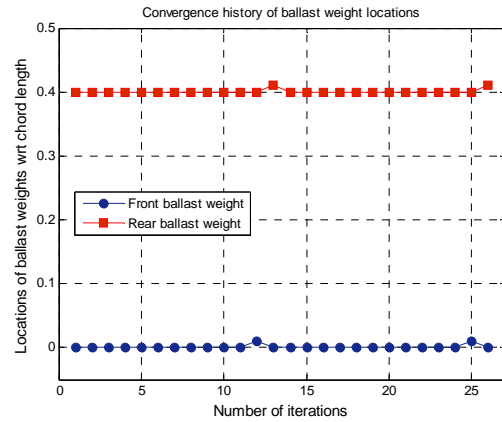
Figure 16 Convergence histories of the ballast weight locations

The convergence history of the two ballast weights is shown in Figure 17. The front and rear ballast weights are suddenly changed at around the iteration numbers 10 and 23, which results in the abrupt changes of the sectional mass per unit length and the 1st leadlag frequency during the optimization iterations as previously observed in Figures 13(a) and 14. However the converged ballast weights are quite similar to the initial values.
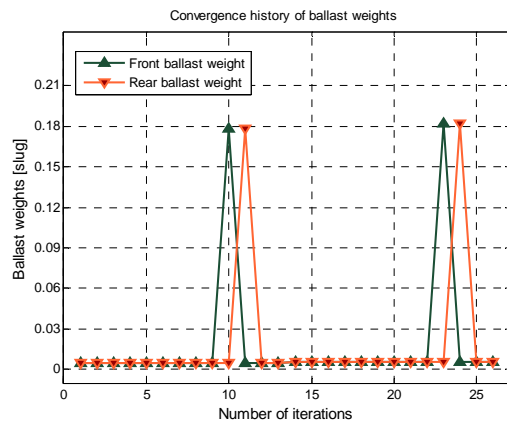
Figure 17 Convergence histories of the ballast weights

Figure 18 shows the convergence history of the locations of the center of gravity of all the sections. Due to the dramatic changes of the two ballast weights during the optimization iterations given in the previous figure, the C.G. locations are also moved to the forward at the 10 and 23th iteration and to the backward at the 11 and 24th iteration. However the locations of C.G. after the convergence are positioned around the quarter chord length, which satisfy the design constraint well.
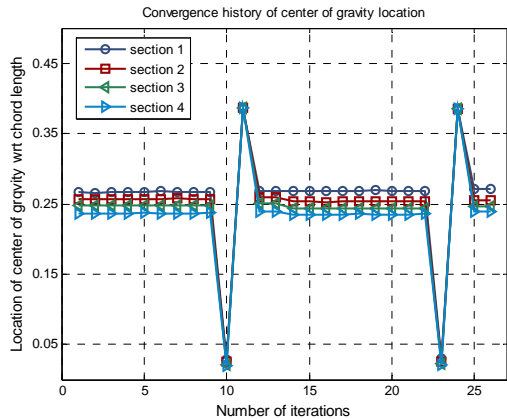
Figure 18 Convergence histories of C.G. locations

Conclusions

This work conducted the optimal design for the variable-twist tiltrotor blade using the SMAHC. The SMAHC was composed of Nitinol alloy wires and S-glass composite matrix. The present variable-twist proprotor was designed based on an existing composite proprotor: the KARI SUAV proprotor however the twist actuation through the SMAHC was designed to be maximized with that a series of design constraints are satisfied. The proposed optimization framework for the design consisted of different numerical tools: an active composite cross-sectional analysis, an automated mesh generator, a nonlinear flexible multibody dynamics analysis, a 3-D strain analysis, and a gradient-based optimizer. The design example showed the tip twist actuation of the variable-twist proprotor was improved by 8% as compared with the reference actuation performance. This optimal design result will make the variable-twist control of the proprotor using the SMAHC be more efficient.

Acknowledgements

References

[1] Nixon, M. W., "Improvements to Tilt Rotor Performance through Passive Blade Twist Control," NASA TM-100583, 1988.

[2] Soykasap, O., "Aeroelastic Optimization of a Composite Tilt Rotor," PhD Thesis School of Aerospace Engineering, Georgia Institute of Technology, 1999.

[3] Ozbay, S., Bauchau, O. A., Dancila, D. S., Armanios, E. A., "Extension-Twist Coupling Optimization in Composite Rotor Blades," 46th AIAA/ASME/ASCE/AHS/ASC Structures, Structural Dynamics and Materials Conference, Austin, Texas, 2005.

[4] Prahlad, H., Chopra, I., "Design of a Variable Twist Tiltrotor Blade Using Shape Memory Alloy Actuators," SPIE – The International Society for Optical Engineering vol.4327, pp.46-59, 2001.

[5] Park, J.-S., Kim, S.-H., Jung, S. N., "Application of Shape Memory Alloy Hybrid Composites for Variable-Twist Proprotors," The American Helicopter Society 66th Annual Forum, Phoenix, AZ, 2010.

[6] Friedman, P. P., "Helicopter Vibration Reduction Using Structural Optimization with Aeroelastic/Multidisciplinary Constraints-A Survey," J. of Aircraft, Vol.28, pp.8-21, 1991.

[7] Walsh, J. L., Young, K. C., Tarzanin, F. J., Hirsh, J. E., Young, D. K., "Optimization Issues with Complex Rotorcraft Comprehensive Analysis," AIAA/USAF /NASA/ISSMO 7th Symposium on Multidisciplinary Analysis and Optimization, St. Louis, MO, 1998.

[8] Celi, R., "Recent Applications of Design Optimization to Rotorcraft," J. of Aircraft, Vol. 36, pp. 176-189, 1999.

[9] Cesnik, C. E. S., Mok, J.-W., Parikh, A. S., Shin, S.-J., "Optimization Design Framework for Integrally Twisted Helicopter Blades," 44th AIAA/ASME/ASCE/AHS/ASC Structures, Structural Dynamics and Materials Conference, Palm Springs, CA, 2004.

[10] Park, J.-S., and Shin, S.-J., "Preliminary Design Optimization on Active Twist Rotor Blades Incorporating Single Crystal Macro Fiber Composites," The American Helicopter Society 63rd Annual Forum, Virginia Beach, VA, 2007.

[11] Choi, S. -W., Kang, Y. -S., Chang, S. -H., Koo, S. -O., Kim, J. M., "Small Tiltrotor UAV Development and Conversion Flight Test," 34th European Rotorcraft Forum, Liverpool, England, 2008.

[12] Brinson, L. C., "One-dimensional Constitutive Behavior of Shape Memory Alloys: Thermomechanical Derivation with Non-Constant Material Functions and Redefined Martensite Internal Variable," Journal of Intelligent Material Systems and Structures vol.4, pp.229-242, 1993.

[13] Tanaka, K., "A Thermomechanical Sketch of Shape Memory Effect: One Dimensional Tensile Behavior," Res Mechanica vol.18 pp.251-263, 1986.

[14] Liang, C., Rogers, C. A., "One-Dimensional Thermomechanical Constitutive Relations for Shape Memory Materials," Journal of Intelligent Material Systems and Structures, vol. 1, 207-234, 1990.

[15] Park, J. -S., Kim, J. -H., Moon, S. -H., "Vibration of Thermally Post-Buckled Composite Plates Embedded with Shape Memory Alloy Fibers Composite Structures," vol.63, pp.179-188, 2004.

[16] Bailey, B., Snowden, M., Bartley, M., Phelps, A., Lee, M. -K., Kim, J. M., "Design of an Advanced Composite Proprotor Blade for The Tilt-Rotor Smart UAV," American Helicopter Society 62nd Annual Forum, Montreal, Canada, 2006.

[17] Cesnik, C. E. S., Palacios, R., "Modeling Piezocomposite Actuators Embedded in Slender Structures," 44th AIAA/ASME/ASCE /AHS/ASC Structures, Structural Dynamics and Materials Conference, Norfolk, VA, 2003.

[18] Brown, E. L., "Integrated Strain Actuation in Aircraft with Highly Flexible Composite Wings," PhD Thesis Department of Aeronautics and Astronautics, Massachusetts Institute of Technology, 2003.

[19] Bauchau, O. A., DYMORE Manual, http:// www.ae.gatech.edu/people/obauchau/Dwnld/ DymoreManual.pdf, 2007.

[20] Coleman, T. F., and Zhang, Y., "Optimization Toolbox for Use with MATLAB," The MathWorks, Inc., Natick, MA, 1999.

[21] Floros, M. W., Shen, J., Lee, M. -K., Hwang, S. -J., "Loads and Stability Analysis of an Unmanned Tilt Rotor," The American Helicopter Society 62nd Annual Forum, Phoenix, AZ, 2006.

[22] Hodges, D. H., "A Mixed Variational Formulation Based on Exact Intrinsic Equations for Dynamics of Moving Beams," International Journal of Solids and Structures, vol.26, pp. 1253-1273, 1990.

[23] Peters, D. A., He, C. J., "Finite State Induced Flow Models Part II: Three-Dimensional Rotor Disk," Journal of Aircraft, vol.32, pp.323-333, 1995.

[24] Rao, S. S., "Engineering Optimization: Theory and Practice," John Wiley & Sons, Inc., 1996.